

THRUST MEASUREMENT OF DIELECTRIC BARRIER DISCHARGE PLASMA  
ACTUATORS AND POWER REQUIREMENTS FOR AERODYNAMIC CONTROL

by

JOSEPH WILLIAM FERRY

A THESIS

Presented to the Faculty of the Graduate School of the  
MISSOURI UNIVERSITY OF SCIENCE AND TECHNOLOGY

In Partial Fulfillment of the Requirements for the Degree

MASTER OF SCIENCE IN AEROSPACE ENGINEERING

2010

Approved by:

Joshua L. Rovey, Advisor  
Walter Eversman  
Jonathan W. Kimball

© 2010

Joseph William Ferry

All Rights Reserved

## ABSTRACT

Plasma-based aerodynamic actuators are of interest to researchers because they do not require moving control surfaces or a source of pressurized air to modify a flow field. Dielectric barrier discharge (DBD) plasma actuators have the added advantages of simple installation and low power consumption.

DBD plasma actuators are AC devices. This work measured actuator power consumption and thrust production for driving frequencies between 1 and 18 kHz, and for driving voltages of 6 and 9 kV peak to peak. The actuator consumed between 3 and 22 W of power and produced thrust levels between 0.05 and 0.2 mN per meter span. A comparison showed close agreement between the results of this work and those of other researchers. The actuator effectiveness (i.e., thrust produced per watt of power input) was calculated and found to range between 0.017 and 0.11 mN/W.

The continuous power consumption of a DBD actuator-based control system was estimated by modeling the actuators as jet flaps. This work determined the elevator jet flap strength required to trim two small aircraft in flight. First, a 0.5 kg aircraft with 0.76 m<sup>2</sup> wing area required between 0.47 and 2.22 kW of power for trim. A second 3 kg aircraft with 1.27 m<sup>2</sup> wing area required between 13.6 and 54.6 kW of power for trim.

## ACKNOWLEDGMENTS

I would like to thank my advisor, Dr. Joshua Rovey, for all of his advice, his help, and for his understanding when I blew up a transformer. I would like to thank Dr. Walter Eversman and Dr. Jonathan Kimball for serving as my committee members; their advice and help with the project have been much appreciated. I am grateful to all the members of the Aerospace Plasma Lab and the MAE technical shop staff for sharing their time and expertise. Finally, my family and friends have been a source of encouragement without which I would not have made it this far.

## TABLE OF CONTENTS

	Page
ABSTRACT .....	iii
ACKNOWLEDGMENTS .....	iv
LIST OF ILLUSTRATIONS .....	vii
LIST OF TABLES .....	ix
NOMENCLATURE .....	x
SECTION	
1. INTRODUCTION.....	1
1.1. DBD ACTUATOR INTRODUCTION .....	1
1.2. DBD ACTUATOR OPERATION.....	2
1.3. RECENT RESEARCH ON DBD PLASMA ACTUATORS .....	4
1.4. RECENT RESEARCH ON DBD ACTUATOR APPLICATIONS.....	6
2. PROJECT OVERVIEW .....	7
2.1. MOTIVATION OF RESEARCH.....	7
2.2. OBJECTIVE OF RESEARCH .....	7
2.3. EXPERIMENTAL METHOD.....	8
3. EXPERIMENTAL SETUP AND EQUIPMENT .....	11
3.1. ACTUATOR CONFIGURATION.....	11
3.2. POWER SUPPLY.....	12
3.3. ELECTRICAL MEASUREMENT.....	13
3.4. THRUST MEASUREMENT .....	13
4. EXPERIMENTAL OBSERVATIONS AND RESULTS .....	15
4.1. ACTUATOR DEGRADATION AND FAILURE.....	15
4.2. VISUAL OBSERVATIONS OF THE PLASMA DISCHARGE .....	16
4.3. EXPERIMENTAL METHOD AND DATA ACQUISITION.....	20
4.4. POWER CONSUMPTION RESULTS.....	21
4.5. THRUST MEASUREMENT RESULTS.....	23
4.6. RESULTS COMPARISON WITH LITERATURE .....	25
4.7. ACTUATOR EFFECTIVENESS RESULTS .....	26

4.8. ERROR QUANTIFICATION IN THE EXPERIMENTAL RESULTS.....	29
5. ACTUATOR POWER CONSUMPTION TO TRIM AN AIRCRAFT.....	31
5.1. ANALYSIS OUTLINE.....	31
5.2. JET FLAP INTRODUCTION.....	32
5.3. JET FLAP THEORY .....	33
5.4. AIRCRAFT LONGITUDINAL TRIM.....	35
5.5. TRIM CALCULATION RESULTS .....	37
5.6. CURRENT DBD ACTUATOR EFFECTIVENESS.....	39
5.7. POWER REQUIRED TO TRIM THE AIRCRAFT.....	39
5.8. CURRENT ENERGY STORAGE CAPACITY AND SYSTEM FEASIBILITY .....	40
6. CONCLUSIONS .....	41
BIBLIOGRAPHY .....	42
VITA .....	45

## LIST OF ILLUSTRATIONS

	Page
Figure 1.1: DBD actuator layout .....	1
Figure 1.2: Applied voltage and current waveforms for the plasma actuator.....	3
Figure 1.3: Actuator current averaged over 100 waveforms .....	4
Figure 1.4: A DBD actuator operating in (a) mostly diffuse and (b) filamentary discharge modes .....	5
Figure 2.1: Actuator electrical supply and measurement system.....	8
Figure 2.2: Balance beam thrust measurement setup .....	9
Figure 2.3: Experimental setup components.....	10
Figure 3.1: Cross section of the actuator under test .....	11
Figure 3.2: Actuator top view, as mounted on the test stand.....	12
Figure 3.3: Balance beam inside the isolation chamber .....	14
Figure 4.1: New (a) and used (b) plasma actuators.....	16
Figure 4.2: The plasma discharge at 6kVp-p.....	18
Figure 4.3: The plasma discharge at 9 kVp-p.....	19
Figure 4.4: Force trace drift and measurement drop .....	20
Figure 4.5: Actuator power consumption with applied voltage held constant at 6 kV peak to peak .....	22
Figure 4.6: Actuator power consumption with applied voltage held constant at 9 kV peak to peak. ....	23
Figure 4.7: Actuator thrust production with applied voltage held constant at 6kV peak to peak. ....	24
Figure 4.8: Actuator thrust production with applied voltage held constant at 9kV peak to peak. ....	25
Figure 4.9: Actuator thrust production measurements as compared to other authors.....	26
Figure 4.10: Actuator effectiveness with applied voltage held constant at 6 kV peak to peak. ....	27
Figure 4.11: Actuator effectiveness with applied voltage held constant at 9kV peak to peak .....	28
Figure 5.1: The internally blown pure jet flap considered by Spence.....	32
Figure 5.2: A proposed Coanda effect-based trailing edge jet flap.....	35

Figure 5.3: An aircraft free body diagram .....36

**LIST OF TABLES**

	Page
Table 5.1: Aircraft parameters .....	31
Table 5.2: Jet momentum required to trim the aircraft.....	38

## NOMENCLATURE

Symbol	Description
$\mu$	Measurement true mean value
$\bar{x}$	Measurement sample set mean
$x_i$	Measurement single sample value
$S$	Measurement sample set standard deviation
$n$	Number of samples in a measurement sample set
$\alpha$	Angle of attack
$\delta$	Jet flap deflection angle
$i_w$	Wing incidence angle
$\varepsilon_h$	Downwash angle at horizontal stabilizer
$C_\mu$	Jet flap momentum coefficient
$m_j$	Jet flap mass flow rate
$v_j$	Jet flap induced velocity
$q$	Free stream dynamic pressure
$c$	Lifting surface chord
$C_l$	Infinite wing lift coefficient
$C_L$	Finite wing lift coefficient
$F$	Ratio of finite and infinite wing lift coefficients
$AR$	Aspect ratio
$L_{wing}$	Main wing lift
$L_{tail}$	Horizontal stabilizer lift
$M_{wing}$	Moment produced by the main wing
$C_{M,cg}$	Aircraft moment coefficient about the center of gravity
$C_{M,w}$	Main wing moment coefficient, $\alpha=0$
$C_{L,h}$	Horizontal stabilizer lift coefficient
$C_{L,w}$	Main wing lift coefficient
$C_{L,\alpha=0}$	Lift coefficient, $\alpha=0$
$\overline{X}_{cg}$	Nondimensional distance from aircraft datum to center of gravity

$\overline{X_{ac,w}}$	Nondimensional distance from aircraft datum to wing aerodynamic center
$\overline{X_{ac,h}}$	Nondimensional distance from aircraft datum to horizontal stabilizer aerodynamic center
$\eta_h$	Horizontal stabilizer dynamic pressure ratio
$S_h$	Horizontal stabilizer area
$S_w$	Main wing area
$V$	Aircraft flight velocity
$P_{trim}$	Power required to trim the aircraft in steady level flight
$F_{trim}$	Jet momentum required to trim the aircraft in steady level flight
$F/P$	Actuator effectiveness, momentum per unit power input

## 1. INTRODUCTION

This introductory section provides an overview of dielectric barrier discharge (DBD) plasma actuators. The covered subjects include DBD actuator construction, recent research, and operating characteristics of DBD plasma actuators.

### 1.1. DBD ACTUATOR INTRODUCTION

Dielectric barrier discharge plasma actuators are simple devices that include a dielectric layer between two electrodes in a specific arrangement. One electrode is grounded and covered by a dielectric layer and the other electrode is placed on top of the dielectric. These electrodes are designated as the covered and exposed electrodes, respectively. This configuration is shown in Figure 1.1. The dielectric layer can be any substance with insulating properties. The materials commonly used in research are Kapton polymer tape, Teflon tape, quartz glass, and Macor ceramic. The electrodes are typically made of copper foil tape.

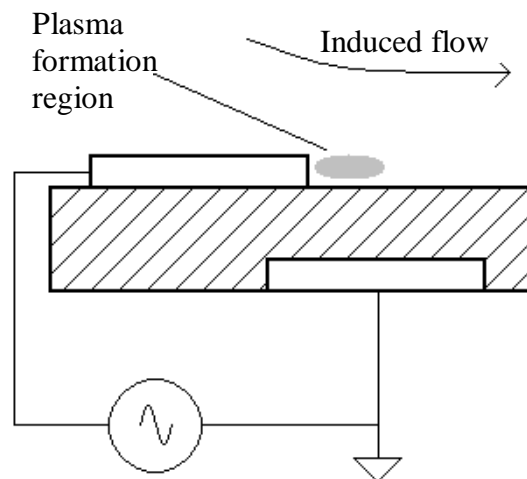


Figure 1.1: DBD actuator layout

To operate the actuator, a high voltage AC signal is applied to the exposed electrode. This causes a plasma discharge to form over the surface of the dielectric between the exposed and covered electrodes. The discharge causes an ionic wind to blow across the actuator. In still air, the actuator induces a flow that draws air toward the surface of the actuator, and accelerates this air downstream in a direction tangential to the dielectric. It is clear that the actuator itself forms and accelerates the plasma; the reaction force on the actuator is small but readily measured.

## 1.2. DBD ACTUATOR OPERATION

Figure 1.2 shows typical applied voltage and current waveforms for an operating plasma actuator. When the current spikes, the plasma has ignited. The plasma ignites and extinguishes itself twice during each AC cycle. During the first half of the cycle the voltage on the exposed electrode is negative-going. This is the forward stroke of the discharge, where electrons jump from the exposed electrode to the surface of the dielectric. These electrons collide with and ionize neutral molecules in the air, forming the plasma. It is important to understand that the voltage applied to the exposed electrode is not the same as the voltage across the plasma. As electrons build up on the surface of the dielectric, they reduce the potential difference across the plasma. The plasma quenches once the applied voltage is no longer negative-going.

The actuator enters its backward stroke once the applied voltage is positive-going. The electrons on the dielectric surface are now pulled back to the exposed electrode. They again collide with and ionize neutral particles, and the plasma ignites for the second time in the AC cycle. The plasma quenches again once the voltage is no longer positive-going.

The electrons jump back and forth between the exposed electrode and the dielectric surface in microdischarges, which are represented by the spikes in the current waveform. These microdischarges are conductive streamers that form and carry electrons between the exposed electrode and the dielectric surface. To the naked eye the plasma appears diffuse, but it is actually formed of many streamers that are random in nature. This has been investigated by other authors using high-speed photography.<sup>1</sup> The

streamers form and quench quickly because the dielectric barrier prevents them from transitioning to an arc discharge. This property is responsible for the non-equilibrium and non-thermal nature of the DBD plasma.

The plasma microdischarges are very different in the forward and backward discharges. In the forward stroke, there are more microdischarges; each microdischarge is more diffuse and carries less charge to the dielectric surface. In the backward stroke, there are fewer microdischarges; each microdischarge is more intense and carries more charge back to the exposed electrode. This is seen in Figure 1.2. Each current spike in the figure represents a microdischarge (or collection of microdischarges). The forward stroke microdischarge current spikes are much smaller than the backward stroke microdischarge current spikes. It should be noted that while the backward stroke current spikes are much larger than the forward stroke current spikes, the average current magnitudes for each half of the discharge are equal. This is more easily seen in Figure 1.3.

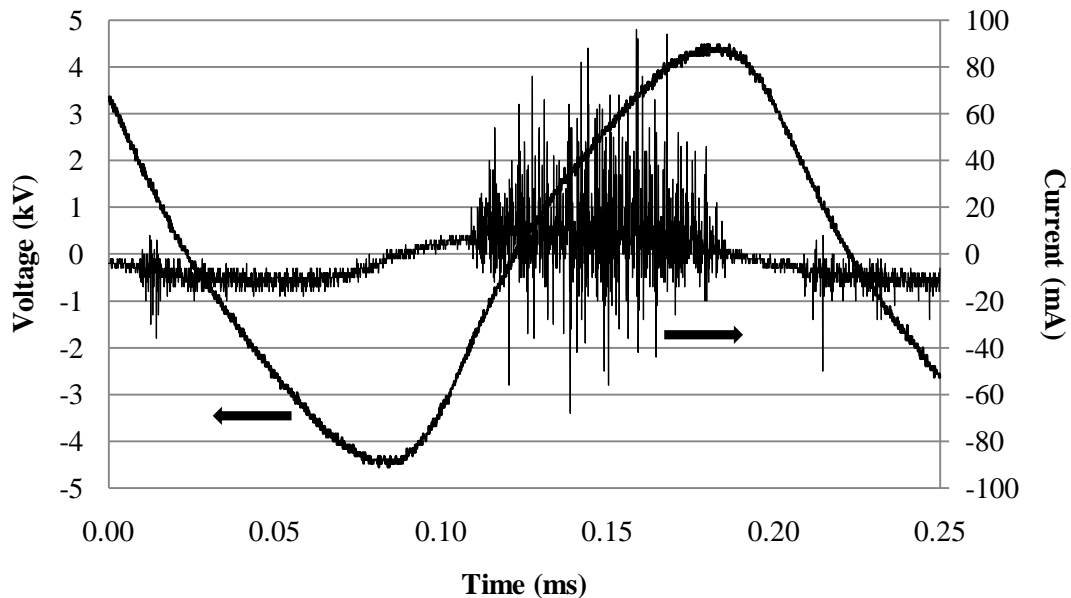


Figure 1.2 Applied voltage and current waveforms for the plasma actuator

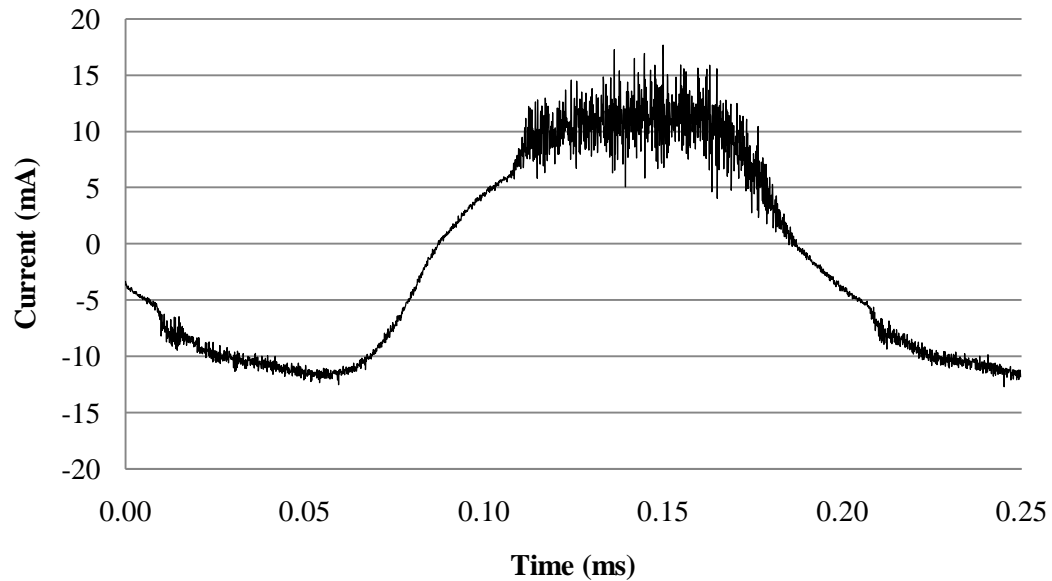


Figure 1.3 Actuator current averaged over 100 waveforms

As the applied voltage and operating frequency are increased, the actuator can saturate and transition to a filamentary discharge. When this happens, hot spots form in the discharge. The hot spots are regions of increased plasma density, and can be seen unaided (Figure 1.4). These filaments are macroscopic phenomena; they are not microdischarges.

### 1.3. RECENT RESEARCH ON DBD PLASMA ACTUATORS

DBD plasma actuators have been the subject of intense research recently. A major focus of the published work has been parametric optimization. In these studies authors have investigated how different operating parameters affect the thrust produced by DBD actuators. Enloe and Thomas have parametrically investigated operating voltage, operating frequency, applied waveform shape, dielectric type, and dielectric thickness with the aim of increasing actuator thrust.<sup>2,3</sup> In Enloe's work he found that altering the AC driving voltage waveform has a great effect on the actuator properties.

He drove an actuator with a sawtooth waveform that maximized the time spent in the forward stroke, and compared to a sawtooth of opposite polarity (which maximized the backward stroke) saw a considerable increase in actuator performance for the same power input. He also showed that using a sharper exposed electrode increased actuator performance, which he attributed to the higher electric field produced.

Thomas investigated the effect of different dielectric parameters on the actuator thrust production. He found that using thicker dielectrics allowed the use of higher actuator voltages, which increased thrust production. He also found that using dielectrics with low dielectric constants increased thrust production.

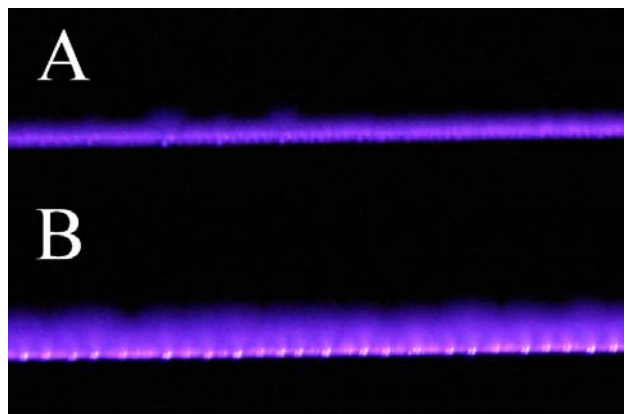


Figure 1.4: A DBD actuator operating in (a) mostly diffuse and (b) filamentary discharge modes. The operating parameters are 9 kHz, 6 kVpp and 8 kHz, 9kVpp, respectively.

With the same goal, Opaitis has investigated DBD operation using pulsed waveforms<sup>4</sup> and Durscher and Roy have investigated novel actuator configurations.<sup>5</sup> Opaitis found that pulsed waveforms were capable of performance similar to conventional sinusoidal-driven actuators at lower voltage levels. Durscher and Roy used a three-electrode configuration to increase actuator efficiency compared to the conventional configuration.

Some authors have investigated the plasma formation and acceleration processes that occur in DBD actuators. Enloe has investigated DBD plasma ignition and spread, and discharge asymmetry.<sup>2,6</sup> Stanfield has investigated ion concentration and temperature in the plasma.<sup>7,8</sup> Enloe and Font have investigated dielectric surface charge build up and actuator force generation.<sup>9,10</sup> Each of these has contributed plasma property measurements to the literature. Font found that the presence of oxygen plays an important role in DBD force production. Also, a charge build up occurs on the surface of the dielectric downstream of the exposed electrode. This charge build up can reach a potential of several kilovolts.

#### **1.4. RECENT RESEARCH ON DBD ACTUATOR APPLICATIONS**

There has also been a focus on applications for DBD plasma actuators. This focus has been driven by the many advantages that DBD actuators offer designers. DBD actuators require none of the ducting that is required of traditional blowing or suction actuators. All that is needed is insulated electrical cabling. Additional advantages are the self-limiting nature of the discharge and the low power levels required to operate the device. Actuators with flexible dielectrics can be made to fit any surface shape. All of these reasons have contributed to a rapidly growing body of experimental work which focuses on specific applications for DBD actuators.

Some of the applications investigated include an active stall detection and control system,<sup>11</sup> bluff body noise control,<sup>12</sup> plasma-enhanced combustion,<sup>13</sup> jet mixing enhancement,<sup>14</sup> high angle-of-attack separation control,<sup>15</sup> high angle-of-attack roll control,<sup>16</sup> turbine blade separation control,<sup>17</sup> DBD microthrusters,<sup>18</sup> turbine tip gap flow control,<sup>19</sup> and other air flow control applications.<sup>20-24</sup> Other developments in DBD actuator research have been summarized in a review article by Corke, Enloe, and Wilkinson.<sup>25</sup>

## **2. PROJECT OVERVIEW**

This section provides a rationale and objective for the current work, to examine the feasibility of using DBD actuators in a plasma-based control system. This section also provides an overview of the experimental setup used in the work.

### **2.1. MOTIVATION OF RESEARCH**

While plasma actuators are not yet capable of actuating high Reynolds number flows, actuator effectiveness has increased greatly through recent research efforts. It is likely that the first flight systems using DBD plasma actuators will be small remote vehicles operating at low Reynolds numbers. The light weight, simplicity, and fast reaction times of the actuators naturally lend themselves to this application. However, in any flight application the power supply and actuators must be considered together as a unit. The actuator driving circuitry must include an energy storage system, a signal generator, and a high-voltage step up stage.

As the actuator power requirements increase, the weight of this power supply must necessarily also increase. Increased energy storage, heavier cabling, and greater cooling requirements would all contribute to this weight increase. Therefore, reducing the power requirements of the actuator would also reduce the weight of the power supply, and enable the systems to be mounted on smaller vehicles. The motivation for this research is to examine the power requirements for a DBD actuator-based control system.

### **2.2. OBJECTIVE OF RESEARCH**

This work has two main objectives. The first is to perform an experimental study of the efficiency of a DBD plasma actuator. The actuator thrust and power consumption are measured for this calculation. This has been done previously, but this work increases the base of experimental data available. The second objective is to examine the problem of a plasma actuator-based control system, and to estimate the power required for such a system to trim a small aircraft in level flight. For a stable aircraft in level flight the only

control requirement is the elevator trim. Therefore this power requirement would be an adequate estimate of the control system power requirement in flight.

### 2.3. EXPERIMENTAL METHOD

To investigate the plasma actuator thrust and power consumption, the experimental setup needed to meet three requirements. First, the plasma actuator needed to be powered by a supply capable of producing a 9kVp-p waveform while supplying 20-30 watts of power. Second, the experiment needed to be able to measure the actual power input to the actuator. Third, the experiment needed to be able to measure the thrust produced by the plasma actuator operation.

The experimental concept used was similar to those used in previous studies.<sup>6</sup> The actuator was powered by an audio amplifier and high-voltage step up transformer. The actuator voltage and current waveforms were measured by a high voltage probe and a Pearson current monitor. The actuator electrical supply and measurement system is shown in Figure 2.1.

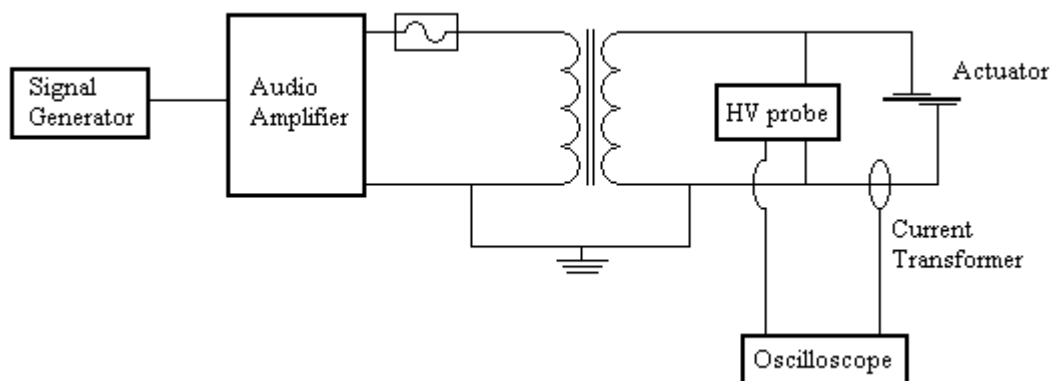


Figure 2.1: Actuator electrical supply and measurement system

The actuator thrust was measured by a balance beam attached to a laboratory mass balance. Because the actuator thrust was extremely small, the balance beam was arranged so that it would mechanically amplify the force produced by the actuator. This arrangement is shown in Figure 2.2. The counterweight allowed the beam to be balanced so that the scale was not overloaded. The actuator power wires were made of lightweight, flexible wires and attached at the balance beam point of rotation.

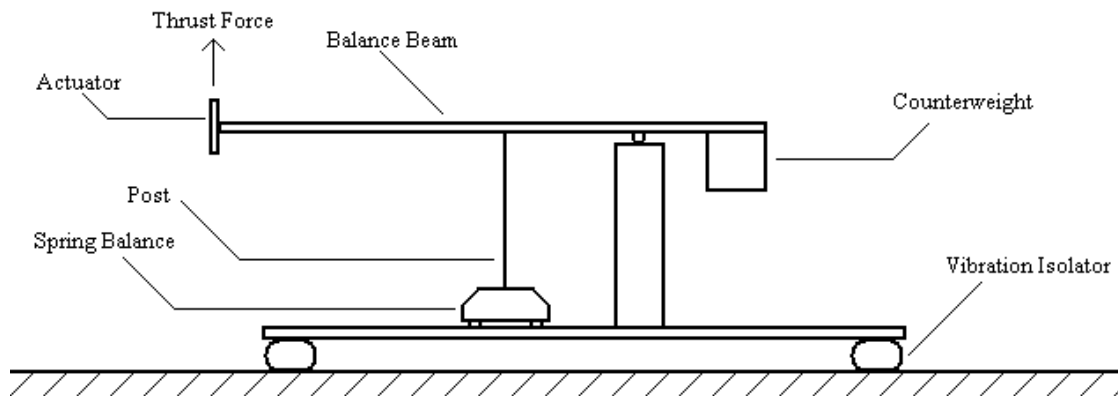


Figure 2.2: Balance beam thrust measurement setup

Figure 2.3 shows the test setup as assembled. The balance beam, scale, actuator wiring, transformer, HV probe, and current sensor are shown. The waveform generator, amplifier, and oscilloscope are not shown.

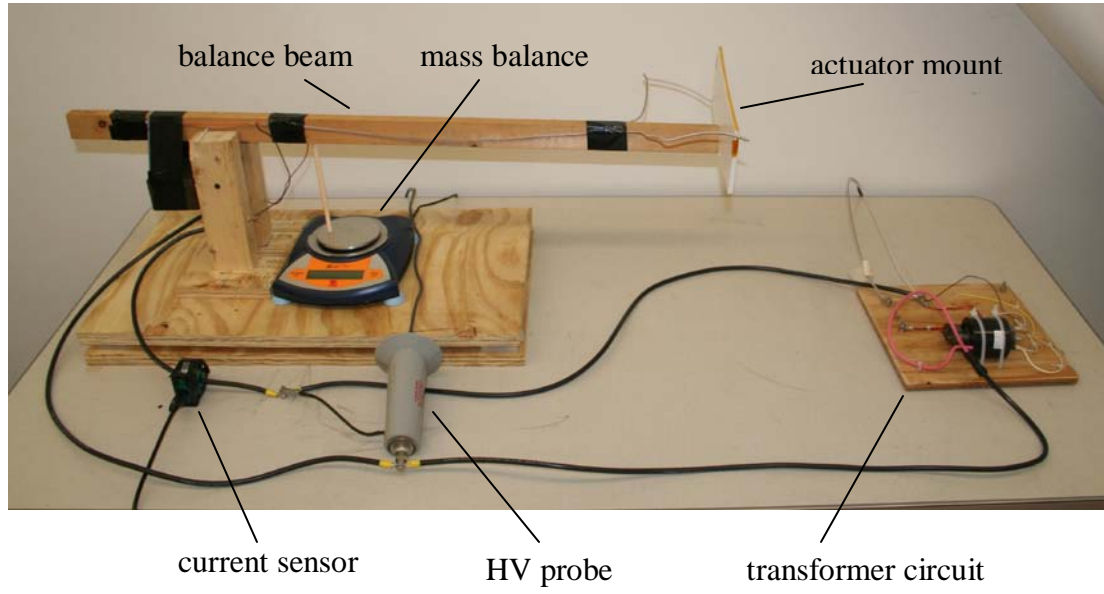


Figure 2.3: Experimental setup components. The oscilloscope, waveform generator, and amplifier are not shown.

### 3. EXPERIMENTAL SETUP AND EQUIPMENT

This section provides the details of the experimental setup. It provides the details of each piece of equipment used in the experiment. Specifically, this section covers the actuator construction, power supply equipment, electrical measurement equipment, and thrust measurement equipment.

#### 3.1. ACTUATOR CONFIGURATION

The actuators used in this study were constructed by hand, and used copper tape electrodes with a Kapton tape dielectric. The dielectric was constructed by layering three pieces of Kapton on top of each other, which resulted in a dielectric thickness of 0.2 mm. The electrodes were positioned so that the electrodes did not overlap each other, but the exposed electrode edge lay directly on top of the covered electrode edge (Figure 3.1). The actuators were mounted on a foam-core board substrate. The exposed electrodes were each 25 cm in length, and the covered electrodes were slightly longer than the exposed electrodes (Figure 3.2).

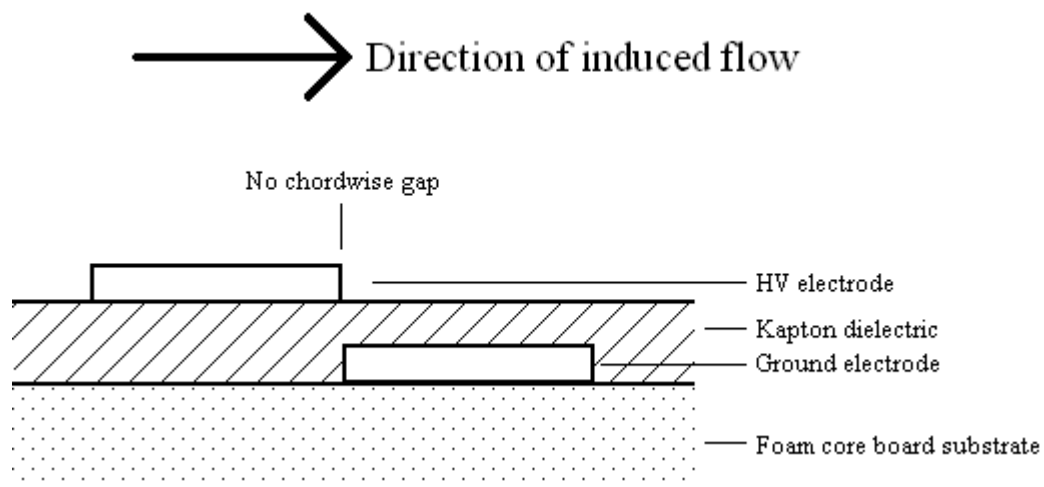


Figure 3.1: Cross section of the actuator under test

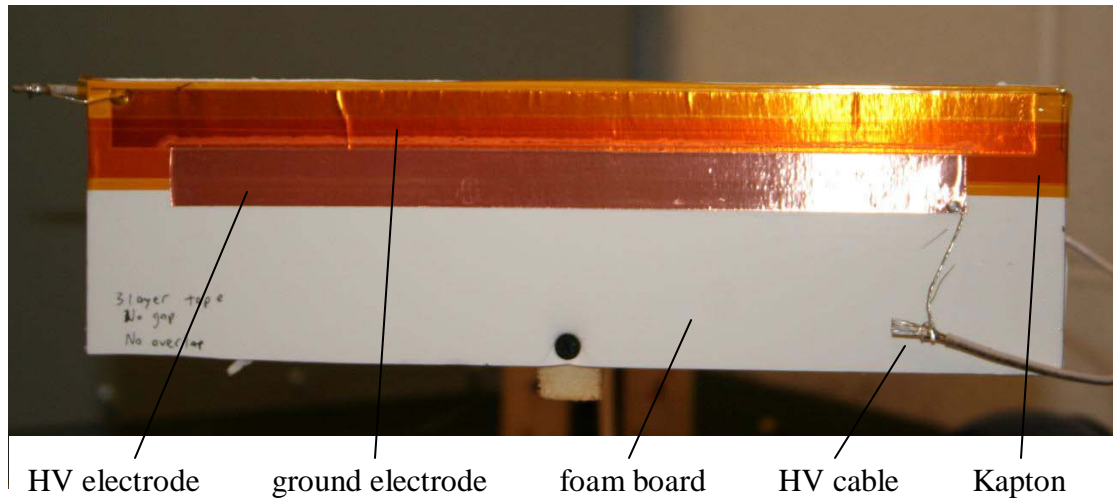


Figure 3.2: Actuator top view, as mounted on the test stand

### 3.2. POWER SUPPLY

The actuator driving circuitry had three main components. A Wavetek Model 110 analog function generator was used to drive a Crown CE2000 amplifier. The function generator was used to define the waveform shape, signal amplitude, and driving frequency. The CE2000 was a two-channel amplifier and each channel was rated to provide 975W to a 2-ohm load. The amplifier was operated in a dual mono configuration, so that one of the amplifier channels drove the actuator while the other was unused. The amplifier output drove a transformer which stepped up the voltage to kilovolt levels.

Two separate transformers were used to drive the actuator across different frequency ranges. The first was a Corona Magnetics CMI-6495 transformer with a 1:100 turns ratio. It is rated for a 4000 V, 0.03 A output. Its self resonant frequency was near 3 kHz, and it was used to drive the actuator for frequencies between 1-10 kHz. The second transformer was a Corona Magnetics CMI-5012-1. It had a 1:137.5 turns ratio, and it was rated for a 5500 V, 0.1 A output. Its self resonant frequency was 6 kHz, and it was used to drive the actuator for frequencies between 10-18 kHz. Both of these transformers were protected by a 5 A fuse between the amplifier and the transformer primary coil.

### 3.3. ELECTRICAL MEASUREMENT

In the experiment, a common ground was provided between the amplifier output, the transformer primary coil, and the transformer secondary coil. To accurately measure the actuator driving voltage, a Tektronix P6015 high voltage probe was used to measure the voltage between the actuator exposed electrode and ground. The probe was physically located as close to the electrode as possible, to eliminate the effects of corona on long wire runs. The probe -3 dB attenuation point is 75 MHz, so it was sufficient to measure the 1-18 kHz applied voltage waveforms.

The actuator current was measured by placing a Pearson electronics model 4100 current monitor around the actuator ground wire. This type of current monitor (a Rogowski coil) is essentially a coil of wire that encircles the wire under test, and it was designed so that the voltage induced in the monitor wire is proportional to the current through the test wire. The current was measured through the ground wire because capacitive effects between the monitor and high voltage wire would introduce error to the measurement if the high voltage line were measured. The current monitor low frequency -3 dB attenuation point was 140 Hz, and the high frequency -3 dB attenuation point was 35 MHz. The current monitor also had a usable rise time of 10 ns. This means that the current monitor was able to accurately measure displacement current at the 1 kHz driving frequency and was also able to capture the microdischarge current spikes produced by the actuator.

The high voltage probe and current monitor were both connected to a Tektronix TDS 2014B 100 MHz oscilloscope. The oscilloscope interfaced with a PC via USB, and a LabVIEW program was used to capture and store each waveform.

### 3.4. THRUST MEASUREMENT

An Ohaus SP-123 mass balance was used to measure the actuator thrust. This balance had a 0.001 gram resolution and could measure a maximum of 120 grams. This corresponds to a  $10^{-6}$  N resolution and maximum measurable force of 1.17 N. Because the actuator thrust was extremely small, a balance beam was used to multiply the actuator force. Most of the balance beam weight was supported by a rolling support that was free

to rotate, and a second support rested on the balance measurement tray. A counterweight was positioned so that the balance was not overloaded. The force measured by the balance was then 4.9 times greater than the actual actuator thrust produced. To power the actuator, two electrical leads had to be attached to the balance beam. So that they would not influence the measurement, these leads were made as lightweight as possible and were attached close to the point of rotation of the beam. With this setup, they exerted a moment on the beam that was as close as possible to zero.

The thrust measurement setup was very sensitive, so that it was possible for ambient air currents to introduce thrust measurement noise that was many times greater than the actual force being measured. To eliminate this noise the entire setup was set inside an isolating chamber, as seen in Figure 3.3. The chamber was large enough so that the actuator would not set up a large scale circulating airflow inside the chamber.

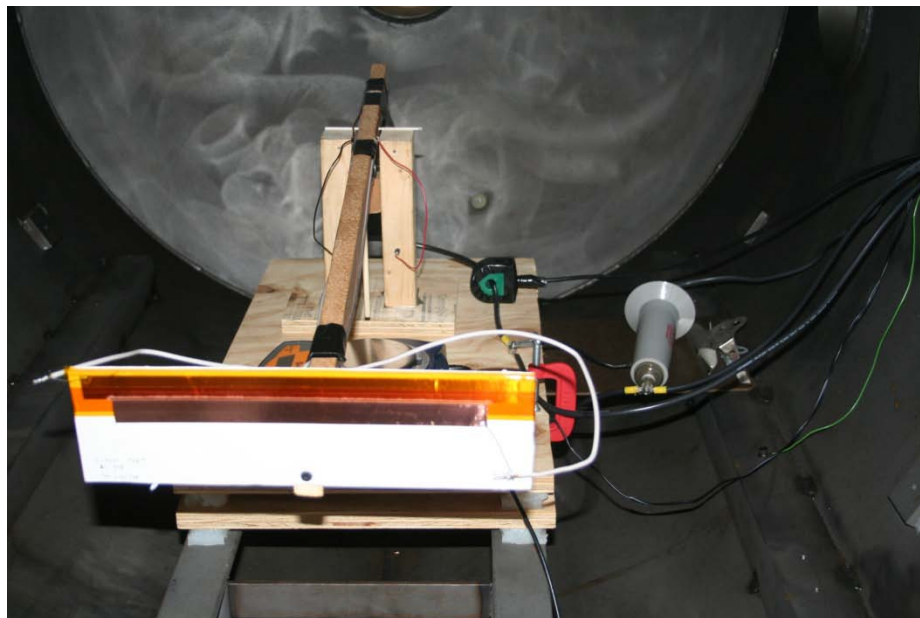


Figure 3.3: Balance beam inside the isolation chamber

## **4. EXPERIMENTAL OBSERVATIONS AND RESULTS**

This section begins with visual observations of the actuator and plasma. It contains the experimental method used in the experiment, and then reports the experimental data gathered. The measurements reported include power measurements, thrust measurements, a comparison of results with other authors, and actuator efficiency calculations.

### **4.1. ACTUATOR DEGRADATION AND FAILURE**

It was observed that the actuators all experienced physical degradation during their operation. The severity of this degradation appeared to be related to the total operating life of the actuator. Actuators with long life spans appeared to have more visible degradation, and actuators operated for just a short time appeared to have minimal degradation.

Disregarding conditions such as applying excessive voltage to an actuator, actuator failures appeared to be due to actuator degradation. It was common for actuators to suddenly fail during experimentation even though the electrical driving voltage and frequency were not being changed during the failure. The voltage and frequency would be set and left constant for several minutes, and the actuator would then fail with no outside interference. Actuator failure always presented itself as arcing through the dielectric barrier, shorting the electrodes. In this situation the power amplifier and transformer were protected by the 5 amp fuse on the transformer primary coil.

One form of physical actuator degradation was erosion of the exposed copper electrode. After prolonged use, the actuators showed erosion of the exposed electrode next to the plasma formation region. The electrode had a smooth edge before operation and a rough or jagged appearance after use. Another kind of degradation presented itself as a discoloration on the surface of the dielectric downstream of the exposed electrode. The Kapton dielectric started as a clear orange-brown color, and after use the dielectric appeared to have a light-colored opaque discoloration downstream of the plasma formation region. A visual comparison between new and used actuators is shown in

Figure 4.1. The used actuator in this figure had been operated for approximately two hours at 9 kVp-p and varying frequencies.

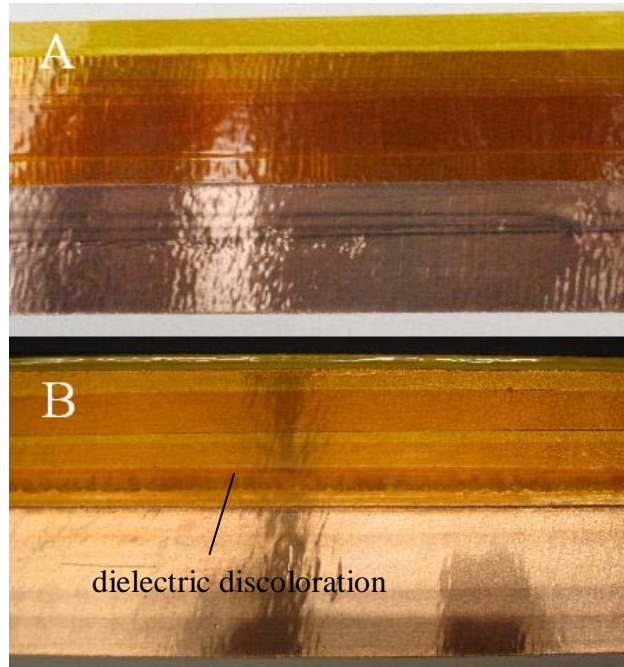


Figure 4.1: New (a) and used (b) plasma actuators. The dielectric discoloration is clearly shown, but the electrode erosion detail is too small to be easily seen here

#### 4.2. VISUAL OBSERVATIONS OF THE PLASMA DISCHARGE

Several visual observations were made of the plasma structure during actuator operation. It is well-known that a diffuse-mode barrier discharge will transition to a highly filamentary discharge as the driving voltage and frequency are increased. The point at which the discharge transitions to the filamentary mode depends upon the electrode spacing, dielectric thickness, and dielectric material. The filamentary mode discharge appears when localized hot spots appear in the plasma. These hot spots appear

to be brighter than other regions of the plasma, because of increased plasma formation in the hot spots.

When the discharge was already in a filamentary mode, increasing the actuator operating frequency increased the number of hot spots in the plasma. With the actuators used in this study, the presence of hot spots also typically indicated that the actuator driving voltage was near the maximum permitted by the dielectric. Therefore, increasing the driving voltage from this point resulted in actuator failure due to dielectric burn-through.

A visual survey of the DBD plasma is useful because the thrust and effectiveness of the plasma actuator heavily depended upon the kind of discharge that was created. As the actuator driving voltage and frequency were increased, the actuator thrust increased whether the discharge was in a diffuse or a filamentary mode. However, when the discharge was in a filamentary mode the actuator efficiency decreased as the driving frequency was increased. Each of the photos in Figures 4.2 and 4.3 was taken by a Canon Rebel DSLR camera. For each photograph, an f/10 aperture and ¼ second shutter speed was used.

It can be seen that when the driving voltage was 6 kVp-p, the discharge was relatively diffuse over the entire range of frequencies used (Figure 4.2). The plasma intensity increased as the driving frequency was increased, but hot spots never formed in the discharge. The difference between Figures 4.2 and 4.3 is significant. Figure 4.3 shows the discharge when the driving voltage was 9 kVp-p. At a driving frequency of 1 kHz, some barely-formed hot spots were observed. When the frequency was increased to 3 kHz, hot spots formed and were plainly visible. As the frequency was increased to 9 kHz, the number and intensity of the hot spots increased significantly. At these higher frequencies, the discharge was highly filamentary.

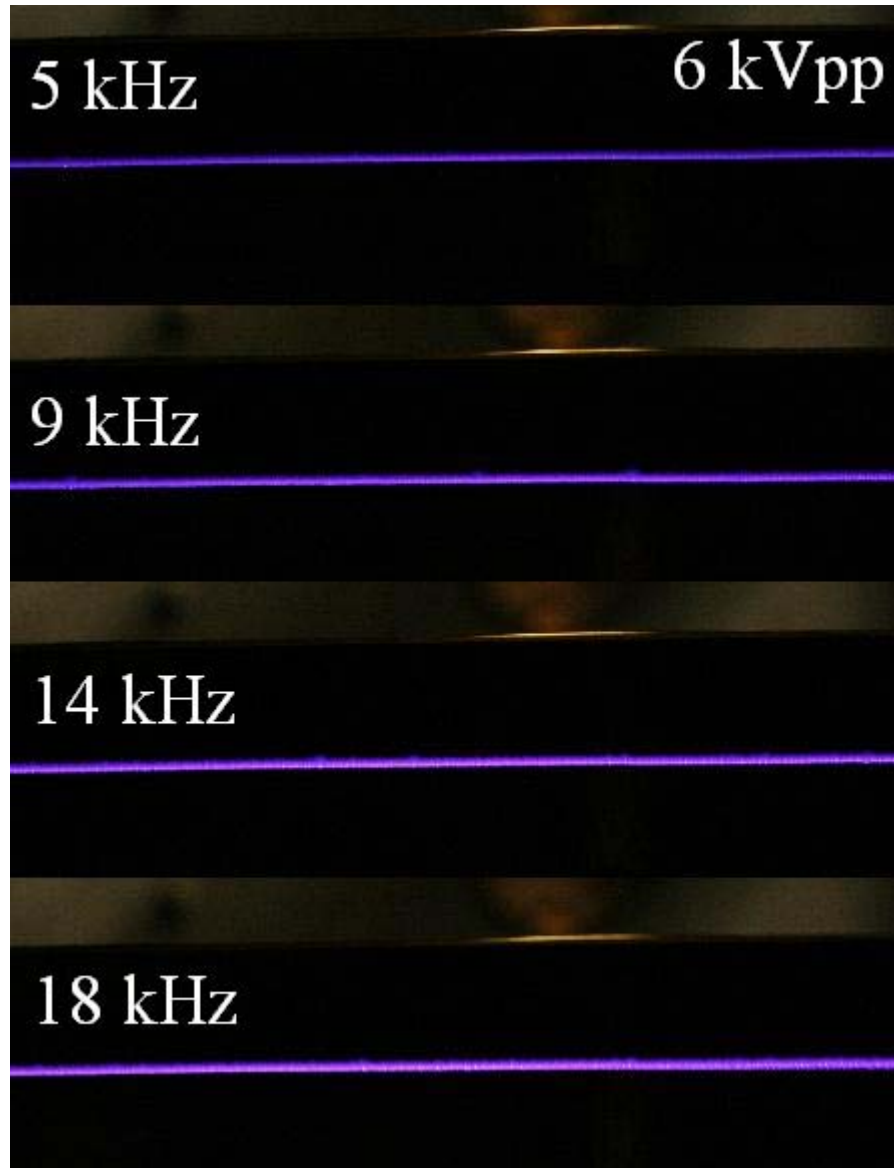


Figure 4.2: The plasma discharge at 6kVp-p. It increases in intensity as the voltage is held constant and the driving frequency is increased. There are very few hot spots at a 6 kVp-p driving voltage



Figure 4.3: The plasma discharge at 9 kVp-p. It increases in intensity as the voltage is held constant and the driving frequency is increased. There are no significant hot spots at 1 kHz and 9 kVp-p, but they form and quickly increase in number with increasing frequency

### 4.3. EXPERIMENTAL METHOD AND DATA ACQUISITION

During the experiment, three separate sets of data were recorded. The first of these was the actuator thrust measurements. A LabVIEW program was used to record the thrust data. It recorded the force balance readout approximately five times per second, as fast as the scale circuitry allowed.

It was found that the force measurement would drift over time. This drift displayed unusual characteristics, and one significant observation was that the measurement drifted in one direction with the actuator off and in the opposite direction with the actuator on (Figure 4.4). For this reason it is believed that the drift was related to the actuator operation in some way. Other experiments showed that the drifting was also related to the room ambient conditions. The cause of this drifting is unknown, but it prevented the acquisition of thrust measurements simply by taking a quiescent value and a second measurement with the actuator on.

To eliminate the drift effect from the measurements, the actuator thrust measurement was taken by turning off the actuator and measuring the change in force that resulted. Five separate force readings were taken for each measurement.

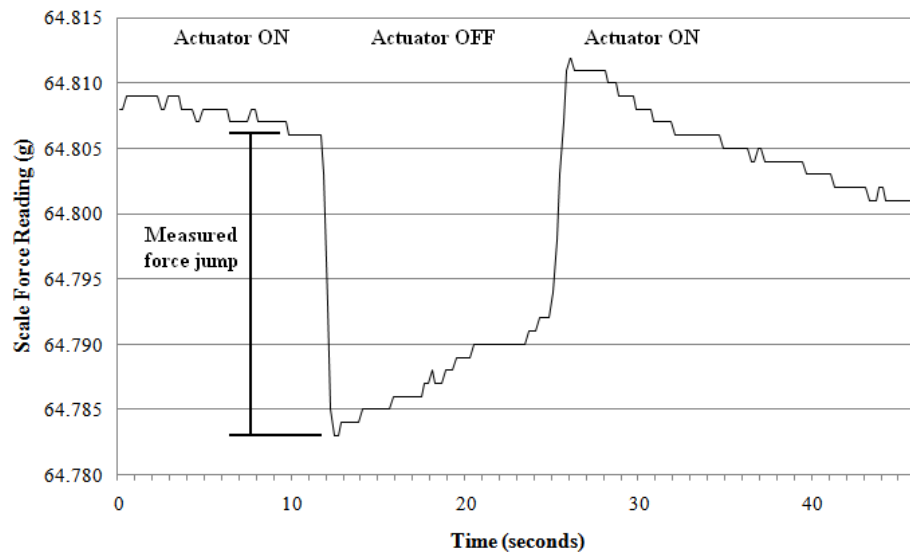


Figure 4.4: Force trace drift and measurement drop

The second and third measurements taken were the actuator applied voltage and current measurements. Again a LabVIEW program was used to simultaneously acquire and store both current and voltage waveforms. For each measurement, 100 separate voltage and current waveforms were recorded.

To summarize, each measurement followed this procedure:

1. Set the actuator driving frequency
2. Use LabVIEW to begin recording force measurements from the mass balance
3. Turn on the power amplifier
4. Increase the voltage amplitude to the desired value
5. Use LabVIEW to record 100 voltage and current waveforms
6. Quickly decrease the voltage amplitude to 0 V
7. Allow the scale reading to settle
8. Repeat steps 4-7 four more times
9. Turn off the power amplifier
10. Stop and save the LabVIEW force measurement record

#### **4.4. POWER CONSUMPTION RESULTS**

Actuator power consumption is presented in this section. Figures 4.5 and 4.6 show how the actuator power consumption changes as the applied frequency changes. The applied voltage in each chart is held constant at 6 kV peak to peak and 9 kV peak to peak, respectively. The points on each chart represent the mean power consumption, calculated from five sets of 100 waveforms each. The error bars shown are the 99% confidence interval for the measurement average.

The experimental apparatus did not directly measure power input, but it recorded the driving voltage and current waveforms. To calculate the power the voltage and current waveforms were multiplied point-by-point, which gave a power waveform. The power input was calculated by averaging the power waveform over one or two periods of the driving frequency.

There are two distinct regions in Figure 4.5. For driving frequencies between 5 – 10 kHz the power consumption increases linearly as the driving frequency increases. There is a small discontinuity between 10 and 11 kHz, and between 11 – 18 kHz driving frequencies the power consumption begins to level off. The discontinuity is explained by the fact that two different power transformers were used to power the actuator. One transformer powered the actuator between 5 – 10 kHz, and the second transformer powered the actuator between 11 – 18 kHz. The transformers that were used are highly resonant devices, and when operated away from their self resonant frequency, the driving voltage waveforms were not perfect sine waves.

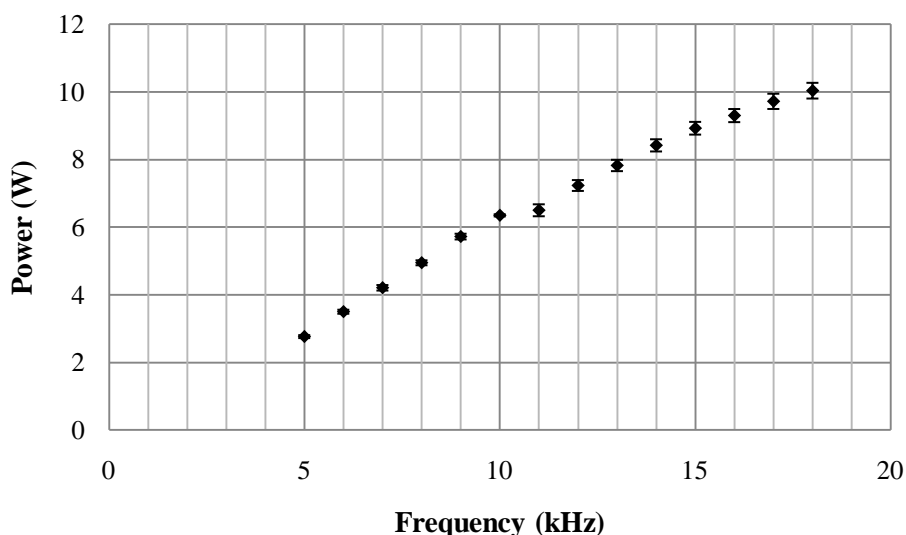


Figure 4.5: Actuator power consumption with applied voltage held constant at 6 kV peak to peak. The Error bars shown are the measurement 99% confidence interval.

Each transformer provided a slightly different driving voltage waveform, which altered the plasma discharge characteristics. When the discharge was modified, the power consumption also changed. It is clear then that distortions of the applied voltage

waveform are a source of bias error in the experiment. In Figure 4.6 no discontinuity is present, because the same transformer powered the actuator for all of the measurements. At the higher driving voltage it is again observed that the power consumption increased linearly with the driving frequency.

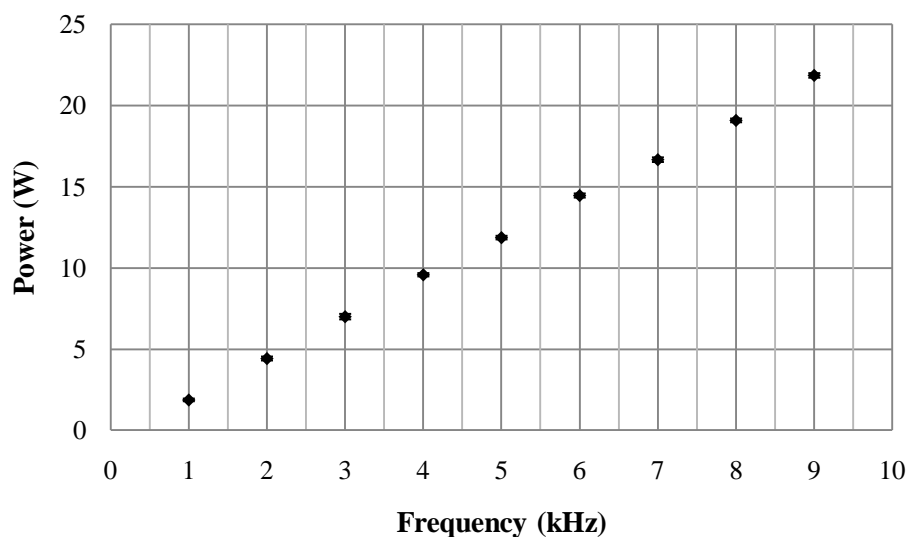


Figure 4.6: Actuator power consumption with applied voltage held constant at 9 kV peak to peak. The Error bars shown are the measurement 99% confidence interval.

#### 4.5. THRUST MEASUREMENT RESULTS

Measured actuator thrust is presented in this section. Figures 4.7 and 4.8 show how the actuator thrust changes as the applied frequency changes. The applied voltage in each chart is held constant at 6 kV peak to peak and 9 kV peak to peak, respectively. Each data point represents the average thrust value over five separate trials. The error bars shown are the 99% confidence interval for the measurement average.

Figure 4.7 shows the actuator thrust levels when the applied voltage is held constant at 6 kV peak to peak. The error bars appear to be quite large because the

resolution of the overall experimental setup was about 0.008 mN/m. This is an order of magnitude smaller than the lowest thrust measurement. There are no significant features on this chart because the discharge was operating in the diffuse mode over the entire range of measurement. Therefore, the effects of the transition to filamentary mode discharge are not seen here. The discontinuity that was seen in Figure 4.5 is not present here. However, the discontinuity may be masked by the greater effects of random error in this set of data.

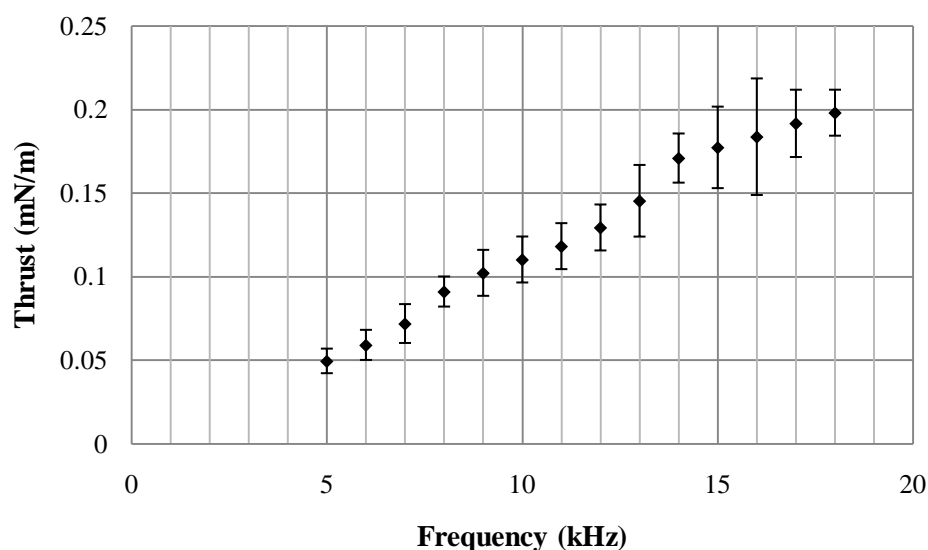


Figure 4.7: Actuator thrust production with applied voltage held constant at 6kV peak to peak. The Error bars shown are the measurement 99% confidence interval.

Figure 4.8 shows the actuator thrust levels when the applied voltage was held constant at 9 kV peak to peak. There are no significant features on this chart because the actuator was operating in the filamentary discharge mode over the entire measurement range. The measurements in this chart were taken in two separate sets on two different days, and different actuators were used to take the two sets of data. One actuator was

used for the 1 – 4 kHz range, and a second actuator was used for the 5 – 9 kHz range. This shows that the thrust measurements were relatively insensitive to the small differences between two hand-built actuators.

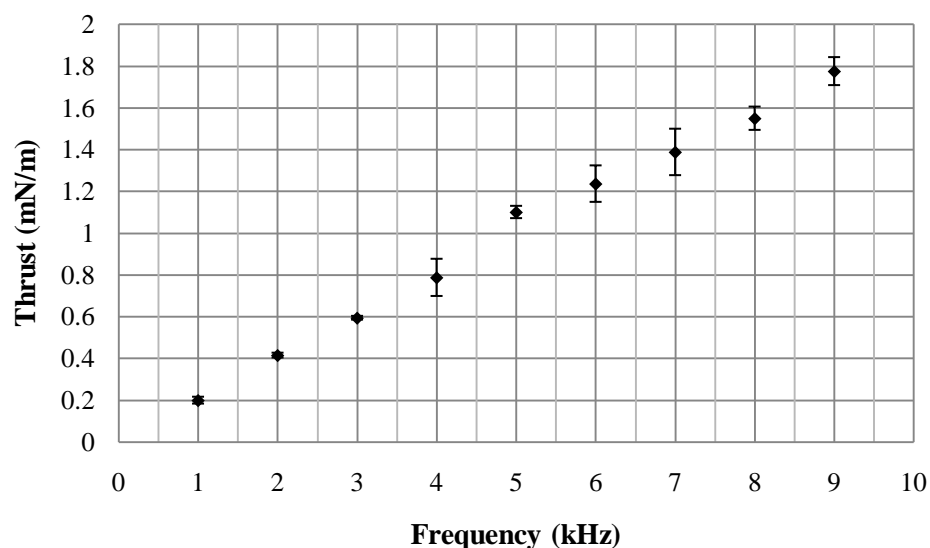


Figure 4.8: Actuator thrust production with applied voltage held constant at 9kV peak to peak. The Error bars shown are the measurement 99% confidence interval.

#### 4.6. RESULTS COMPARISON WITH LITERATURE

There are not yet any theoretical models that can predict actuator performance, so to assess the validity of this experimental data set it was compared with thrust measurements that other authors have published. Figure 4.9 contains thrust measurements taken from the current work as well as literature data. In this figure, the 6 kVp-p data set appears to be almost horizontal. This is because the thrust levels at this voltage are extremely low compared to the other data sets. The 9 kVp-p data set is just below the 12.6 kVp-p measurements reported by Enloe. The difference is smaller than what would be expected, but differences in the driving voltage waveform, actuator

geometry, and dielectric material could account for the difference. The single data point reported by Takagaki does not appear to fit with any of the other data.

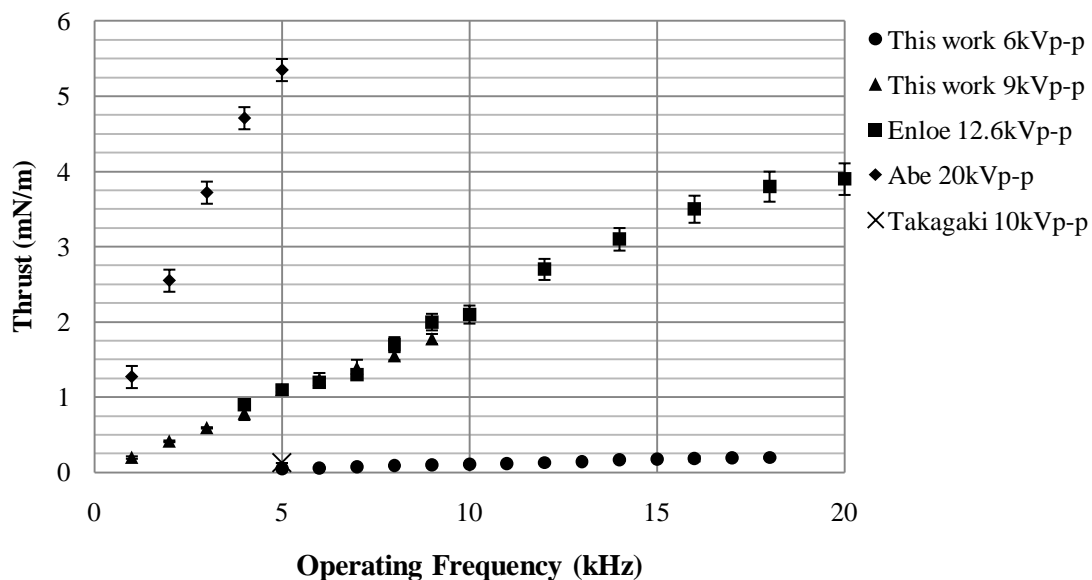


Figure 4.9: Actuator thrust production measurements as compared to other authors. Data reproduced from references 2, 26, and 27

#### 4.7. ACTUATOR EFFECTIVENESS RESULTS

One actuator property that is of interest is how efficiently the actuator converts electrical power into fluid jet power. However, finding the actual power transferred to the fluid would require both a thrust measurement and the induced flow velocity. Measuring the latter quantity is not a trivial problem, so instead of finding the true actuator power conversion efficiency, a quantity called the actuator effectiveness will be used instead. The actuator effectiveness,  $F/P$ , is defined as the actuator static thrust divided by the actuator power consumption. The physical meaning of an effectiveness value is that it shows how much momentum can be added to the flow for one unit of

power input. This quantity has been reported several times in the literature, but has not always been explicitly named.

Calculated actuator effectiveness is presented in this section. Figures 4.10 and 4.11 show how the actuator effectiveness changes as the applied frequency changes. The applied voltage in each chart is held constant at 6 kV peak to peak and 9 kV peak to peak, respectively. Each data point represents the average effectiveness value over five separate trials. The error bars shown are the 99% confidence interval for the measurement average.

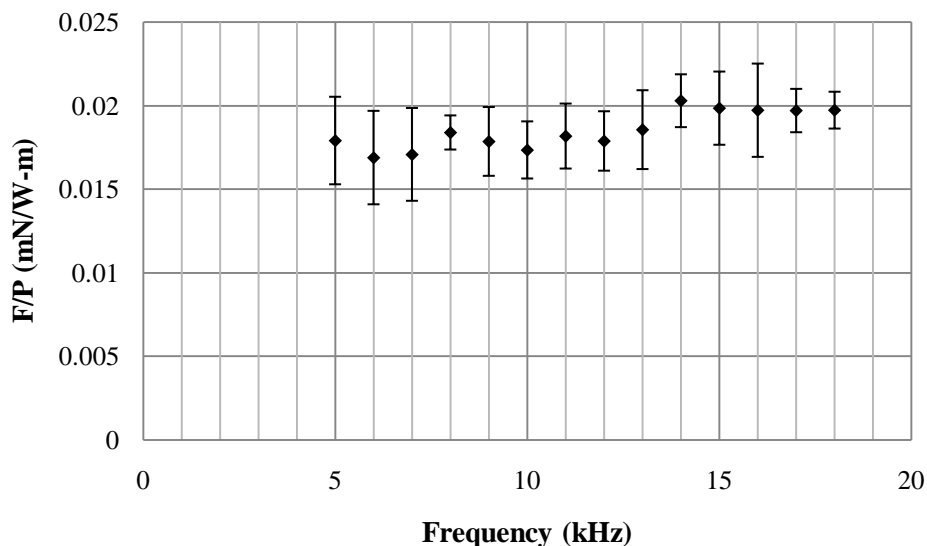


Figure 4.10: Actuator effectiveness with applied voltage held constant at 6 kV peak to peak. The Error bars shown are the measurement 99% confidence interval.

In Figure 4.10, it is seen that the actuator effectiveness is nearly constant with changing frequency. This actuator was operating in the diffuse mode of discharge across the entire range of measurement. There appears to be no significant effect from switching transformers between 10 and 11 kHz. Because it was possible to measure the

power to a very high degree of confidence, the size of the error bars here are dominated by the thrust measurement error.

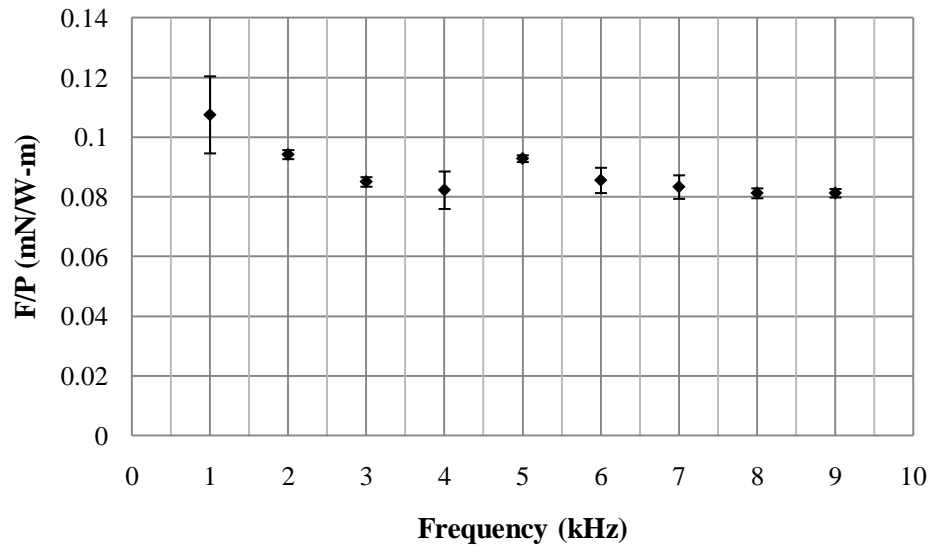


Figure 4.11: Actuator effectiveness with applied voltage held constant at 9kV peak to peak. The Error bars shown are the measurement 99% confidence interval.

In Figure 4.11, one actuator was used to find the effectiveness between 1 – 4 kHz, and a second actuator was used to find the effectiveness between 5 – 9 kHz. It is apparent that for both of these actuators the effectiveness increased as the driving frequency was decreased. However, the trends do not meet between the two data sets. This suggests that the actuator effectiveness is either highly sensitive to small changes in the actuator layout, or that it is sensitive to the ambient conditions.

#### 4.8. ERROR QUANTIFICATION IN THE EXPERIMENTAL RESULTS

Care was taken not to introduce any bias error by poor experimental technique, but because there is no accepted value for the actuator thrust measurements it was not possible to quantify whether any bias error was present in the experimental data.

A major source of random error in the experiment was the waveform generator used to set the driving frequency and voltage. The waveform generator was an analog device, and the voltage and frequency for each measurement was set by hand. When a thrust value at 9 kVp-p and 5 kHz is given, these are the nominal voltage and frequency values. The actual experiment voltage and frequency will have differed slightly from the nominal case. Other sources of possible random error include electrical noise in the measurement setup and physical vibrations causing noise in the thrust measurement.

The random thrust measurement error was quantified by applying Student's t-distribution to find measurement confidence intervals. The t-distribution was used because each mean thrust value was found by averaging five data points. The calculation method taken from reference 28 shows that for a data set consisting of five samples, it is 99% certain that the true mean of the experimental measurement is contained within the interval defined by

$$\mu = \bar{x} \pm 4.604 \frac{S}{\sqrt{5}} \quad (1)$$

Because each average power measurement was based on 100 separate data points, a normal distribution was used to find the confidence interval for these measurements. For a normal distribution and a data set with 100 samples, it is 99% certain that the true mean of the experimental measurement is contained within the interval

$$\mu = \bar{x} \pm 2.575 \frac{S}{\sqrt{100}} \quad (2)$$

For both of these calculations, the sample mean and standard deviation are calculated as

$$\bar{x} = \sum_{i=1}^n \frac{x_i}{n} \quad (3)$$

$$S = \sqrt{\frac{\left( \sum_{i=1}^n x_i^2 \right) - n\bar{x}^2}{n-1}} \quad (4)$$

It is emphasized that these confidence intervals reflect only the random error present in the experimental data. A confidence interval reflects only the spread of data as measured by this experiment. Therefore, a 99% confidence interval does not mean that the actual true value for actuator thrust lies within the interval, but that the average actuator thrust value measured by this experiment will lie within the interval 99 times out of 100. If there is no bias error present in the experiment, then it is 99% certain that the true actuator thrust value lies within the confidence interval.

## 5. ACTUATOR POWER CONSUMPTION TO TRIM AN AIRCRAFT

### 5.1. ANALYSIS OUTLINE

This section presents an analysis of power requirements for a micro air vehicle control system based on DBD plasma actuators. The goal of the analysis was to find the continuous power required to trim the aircraft in steady level flight. The analysis is based upon two conventional micro air vehicles. One of these vehicles is a performance-optimized vehicle with a 1.27 m wingspan and 3 kg mass. The second vehicle is much smaller, with a 0.76 m wingspan and 0.5 kg mass. Table 5.1 gives a physical description of each aircraft.

Table 5.1: Aircraft parameters

	Aircraft 1	Aircraft 2
mass	3 kg	0.5 kg
wing area	1.27 m <sup>2</sup>	0.76 m <sup>2</sup>
tail area	0.064 m <sup>2</sup>	0.017 m <sup>2</sup>
tail chord	0.15 m	0.076 m
stall velocity	10.7 m/s	10.97 m/s
static margin	16.6%	19.5%

The analysis proceeds as follows. First, the jet flap concept is introduced and its applicability to the problem at hand is demonstrated. Jet flap operation and governing equations are discussed. Next, the aircraft longitudinal trim problem is presented and solved for the elevator jet strength required to trim the aircraft in level flight. Last, the power requirement for these flight conditions is calculated using current experimental data.

## 5.2. JET FLAP INTRODUCTION

Powered pneumatic flow control technology was first investigated as early as the 1930s. While the implementation has taken many forms, jet flap systems traditionally feature a source of high-pressure air which can be blown across a conventional control surface or used to create a pure air jet. If the jet issues from the airfoil directly, it is called an internally blown flap. Figure 5.1 shows a schematic of a pure jet flap that was used to construct the first theoretical models of jet flap aerodynamics.

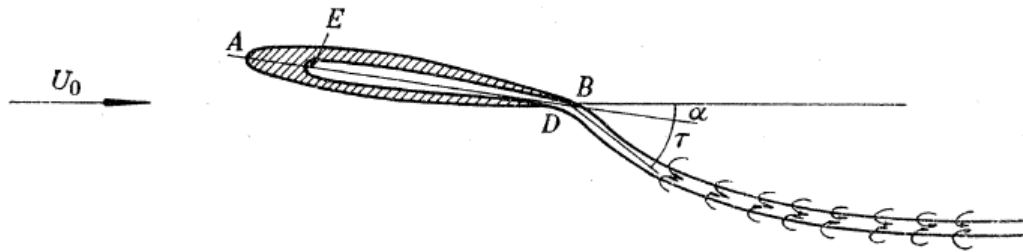


Figure 5.1: The internally blown pure jet flap considered by Spence. Reproduced from reference 29

Korbacher<sup>30</sup> provides an overview of jet flap operation and application to V/STOL flight. Jet flap systems operate on the principle of supercirculation. When the trailing edge jet is sufficiently strong, the Kutta condition at the trailing edge is relaxed. That is, the point in the flow where circulation goes to zero is pushed aft of the airfoil trailing edge.<sup>31</sup> The effect is similar to extending the airfoil chord. With an angled jet, the flow can be turned as well, increasing the effective camber of the airfoil. Because of these effects, the lift gained can be much greater than the jet thrust. Using jet flaps, wind tunnel experiments have achieved finite-wing lift coefficients greater than seven.<sup>32</sup> For V/STOL flight, the advantage of such a system is apparent.

### 5.3. JET FLAP THEORY

Spence<sup>29</sup> first formulated a two-dimensional inviscid jet flap theory in 1956; Maskell and Spence presented a three-dimensional theory in 1959.<sup>33</sup> This work is based upon a textbook treatment of the jet flap by McCormick,<sup>31</sup> which is based on the original work by Spence and Maskell.

A question that needs to be addressed is whether the jet flap theory is applicable to the jets produced by DBD plasma actuators. Traditional jet flaps are positive mass flux devices which work by injecting a jet into the flow, while DBD plasma actuators are zero mass flux devices which locally accelerate the flow over the airfoil. However, Spence's model appears to be well-suited to analyzing DBD actuator jets. Spence considered a thin jet sheet, seen in Figure 5.1. He constructed the jet by considering the case where the jet thickness approaches zero and the jet exit velocity approaches infinity. In this limit, the jet mass flow rate approaches zero while the jet momentum approaches a finite value. This model describes the situation with a trailing-edge DBD actuator very well. Additionally, later investigations found that the jet flap effect scales with the jet momentum, rather than the jet mass flow rate.<sup>34</sup> These investigations also found that the jet flap effect depended only weakly upon the jet thickness. This implies that the jet flap effectiveness is determined primarily by the distance it extends before it is turned in the direction of the free stream.

The nondimensional jet momentum coefficient,  $C_\mu$ , is the primary factor in determining the jet effect upon the airfoil properties:

$$C_\mu = \frac{m_j v_j}{qc} \quad (5)$$

The quantity  $m_j v_j$  is the jet momentum, and is equal to the reaction thrust produced by the jet. The jet flap theory results here are the result of lifting-line theory applied to jet flaps, and are reproduced from reference 30. The lift coefficient of a pure jet-flapped airfoil is given by:

$$C_l = \left( \frac{\partial C_l}{\partial \delta} \right) \delta + \left( \frac{\partial C_l}{\partial \alpha} \right) \alpha \quad (6)$$

$$\frac{\partial C_l}{\partial \delta} = \left[ 4\pi C_\mu \left( 1 + 0.151 C_\mu^{1/2} + 0.139 C_\mu \right) \right]^{1/2} \quad (7)$$

$$\frac{\partial C_l}{\partial \alpha} = 2\pi \left( 1 + 0.151 C_\mu^{1/2} + 0.219 C_\mu \right) \quad (8)$$

In the case where there is no jet ( $C_\mu=0$ ), it can be seen that the airfoil lift curve slope is then equal to that predicted by traditional lifting-line theory,  $\partial C_l/\partial \alpha = 2\pi$ . An important result of these equations is that a DBD plasma actuator based control system will require some mechanism to turn the jet. It can be seen that if  $\delta=0$ , then the jet will only have the effect of increasing the lift curve slope  $\partial C_l/\partial \alpha$ . For an airfoil with a fixed positive angle of attack  $\alpha>0$  and jet deflection  $\delta=0$ , turning on the jet can increase the section lift, but not decrease it.

Fortunately, there are ways to produce an angled jet flap without resorting to mechanical deflection surfaces. Figure 5.2 presents one possibility. It relies on the Coanda effect to turn the jet through the appropriate angle. Previous investigations have shown the feasibility of using the Coanda effect to turn trailing edge jets through significant angles even for jets with small values of  $C_\mu$ .<sup>35</sup>

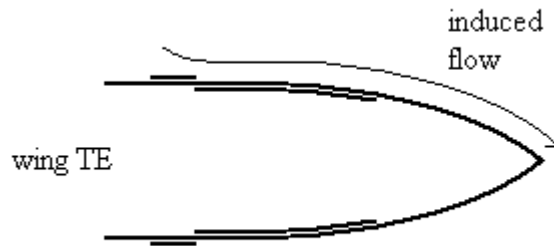


Figure 5.2: A proposed Coanda effect-based trailing edge jet flap. The thick lines represent DBD actuator electrodes

Last in the discussion of jet flap theory is the relation of finite and infinite wing lift coefficients. These are related by a factor,  $F$ , given as

$$F = \frac{C_L}{C_{l_i}} = \frac{AR + 2C_\mu / \pi}{AR + 2 + 0.604C_\mu^{1/2} + 0.876C_\mu} \quad (9)$$

This is an approximation, valid for jet-flapped surfaces with large aspect ratios,  $AR$ , and small jet momentum coefficients,  $C_\mu$ . An implicit relation to find exact values for  $F$  is available, but it is inconvenient to use.

#### 5.4. AIRCRAFT LONGITUDINAL TRIM

For a conventional aircraft, the longitudinal trim problem can be posed as such: given the physical parameters of an aircraft and its forward velocity, what combination of aircraft angle of attack and elevator deflection produce a zero moment about the aircraft center of gravity? For a stable aircraft in straight and level flight the only control force required is an elevator trim deflection. The problem is similar for an aircraft with a plasma jet control system, but an elevator jet momentum is sought instead of an elevator

flap deflection. This simple analysis considers only three forces, which are shown in Figure 5.3.

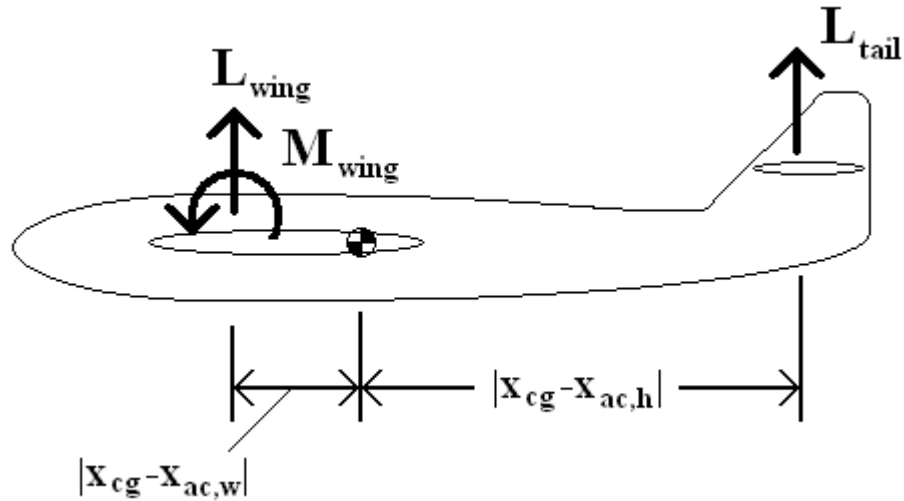


Figure 5.3: An aircraft free body diagram. The main wing lift, main wing moment, and tail lift are shown as forces contributing to the total moment about the aircraft center of gravity

Disregarding any moment contribution by the aircraft propulsion or fuselage, the aircraft moment coefficient about its center of gravity is

$$C_{M,cg} = C_{L,w} (\overline{X}_{cg} - \overline{X}_{ac,w}) + C_{M,w} + \eta_h \frac{S_h}{S_w} C_{L,h} (\overline{X}_{cg} - \overline{X}_{ac,h}) \quad (10)$$

$$C_{L,w} = C_{L,\alpha=0} + \frac{\partial C_{L,w}}{\partial \alpha} (\alpha + i_w) \quad (11)$$

$$C_{L,h} = C_{L,\alpha=0} + \frac{\partial C_{L,h}}{\partial \alpha} \left( \alpha + i_w - \varepsilon_{h,\alpha=0} - \frac{\partial \varepsilon}{\partial \alpha} \alpha_w \right) + \frac{\partial C_{L,h}}{\partial \delta_e} \delta_e \quad (12)$$

For the plasma jet flap elevator, the lift coefficient derivatives are given by equations 7-9 above.

The goal of this analysis is to create a plasma jet-based control system that is equivalent to the conventional control system already installed on the aircraft. With this in mind, the following process was used. First, the trim  $\alpha$  and  $\delta_e$  were calculated for the conventional aircraft configuration, at the free stream velocity of interest. Then the free stream velocity and aircraft angle of attack were held constant, and the jet momentum coefficient required to satisfy the trim condition ( $C_{M,cg}=0$ ) was found. For these calculations, it was assumed that the plasma jet deflection  $\delta=\pm 10^\circ$ .

## 5.5. TRIM CALCULATION RESULTS

These results are summarized in Table 5.2. There are three conditions of primary interest for trimmed flight. These conditions are trimmed flight at  $V=V_{stall}$ , trimmed flight during cruise, and trimmed flight at  $V=V_{max}$ , the maximum attainable velocity in straight and level flight. Flight at the stall velocity and maximum velocity represent the conditions where the maximum elevator control inputs are required. The tail incidence angle for both aircraft was set so that no elevator input was required at the cruise velocity of 16 m/s. The maximum velocity for both aircraft was assumed to be 33.5 m/s.

Table 5.2: Jet momentum required to trim the aircraft

		V (m/s)	$\alpha$ (degrees)	$\delta$ (degrees)	$C_{\mu,trim}$	Jet momentum (N/m)
$V_{stall}$	Aircraft 1	10.7	8.77	-10	0.509	5.47
	Aircraft 2	10.97	11.73	-10	0.158	0.887
$V_{max}$	Aircraft 1	33.5	-5.12	10	0.207	21.856
	Aircraft 2	33.5	1.25	10	0.003	0.189

The first condition to be considered is flight at 16 m/s, max L/D cruise velocity. The tail incidence angle for both aircraft were chosen so that the aircraft is already trimmed at this velocity, so no control input is required and the momentum coefficient  $C_{\mu,trim}=0$ .

Next, flight at  $V=V_{stall}$ . For aircraft 1, the free stream velocity is 10.7 m/s,  $\alpha_{trim}=8.77^\circ$ ,  $\delta=-10^\circ$  and  $C_{\mu,trim}=0.509$ . This yields a plasma jet momentum of 5.470 N/m. For aircraft 2, the free stream velocity is 10.97 m/s,  $\alpha_{trim}=11.73^\circ$ ,  $\delta=-10^\circ$  and  $C_{\mu,trim}=0.158$ . This yields a plasma jet momentum of 0.887 N/m

Last, flight at  $V=V_{max}=33.5$  m/s is considered. For aircraft 1,  $\alpha_{trim}=-5.12^\circ$ ,  $\delta=+10^\circ$  and  $C_{\mu,trim}=0.207$ . This corresponds to a plasma jet momentum of 21.856 N/m. Given that the horizontal stabilizer span is 0.43 m, the total thrust produced by the plasma jet would be equal to 9.4 N. This is roughly 1.4 times the thrust produced by the aircraft engine at this velocity. Obviously, a more comprehensive analysis would need to take this factor into account. For aircraft 2,  $\alpha_{trim}=1.25^\circ$ ,  $\delta=+10^\circ$  and  $C_{\mu,trim}=0.00362$ . This corresponds to a jet momentum of 0.189 N/m.

It should be noted that these high jet strengths are required due to the unique physical operation of jet flaps. A close examination of equations 3-5 shows that increasing the momentum coefficient increases both  $\partial C_L/\partial \alpha$  and  $\partial C_L/\partial \delta$ . A large positive angle of attack requires a negative jet deflection for trim, and a large negative angle of attack requires a positive jet deflection for trim. It is only at small free stream incidence angles that the two terms are complimentary. For an actual application, it

would be desirable to make the jet deflection angle as large as is practical. This would allow the aircraft to be trimmed with the smallest possible jet momentum.

## 5.6. CURRENT DBD ACTUATOR EFFECTIVENESS

As discussed above, the actuator effectiveness is defined as the actuator thrust produced per unit power input. Experimental data shows that this parameter is dependent upon many different factors, including the actuator applied voltage, operating frequency, applied voltage waveform, electrode geometry, dielectric constant and dielectric thickness.

The highest actuator effectiveness achieved in experiment in the present effort is 0.107 mN/W-m. Enloe<sup>1</sup> reports actuator effectiveness as high as 2 mN/W-m. Thomas<sup>2</sup> reports thrust and power data, from which the actuator effectiveness at different operating conditions can be back-calculated to be between 0.2 and 0.4 mN/W-m. Durscher and Roy<sup>4</sup> report an actuator effectiveness of 0.37 mN/W-m using a novel multi-electrode actuator.

It is apparent then that finding a solid trend in these data is difficult. Even more, there is no guarantee that the state of the art actuator effectiveness today will be representative of future plasma actuators that are capable of generating thrust levels 10 to 100 times greater than what is available today. Still, an effectiveness value of 0.4 mN/W-m is representative of the current state-of-the art.

## 5.7. POWER REQUIRED TO TRIM THE AIRCRAFT

Given the jet momentum required to trim the aircraft and the actuator effectiveness, finding the actuator power requirement is a simple calculation. Equation 13 states that the power required to trim the aircraft is equal to the total jet momentum (momentum input per unit power) divided by the actuator effectiveness.

$$P_{trim} = \frac{F_{trim}}{F/P} \quad (13)$$

Based on the trim analysis above, and assuming an actuator effectiveness of 0.4 mN/W-m, aircraft 1 would require 13.6 kW of power to trim the aircraft at its stall velocity, and 54.6 kW of power to trim the aircraft at its maximum velocity. Aircraft 2 would require 2.22 kW of power to trim the aircraft at stall, and 0.47 kW of power to trim the aircraft at its maximum velocity.

## **5.8. CURRENT ENERGY STORAGE CAPACITY AND SYSTEM FEASIBILITY**

Modern remote aircraft use lithium-ion battery packs to store electrical energy. Manganese-based Li-ion batteries currently achieve energy densities around 180 Watt-hours per kilogram. If it is assumed that 50% of the weight of the aircraft is devoted to batteries, then aircraft 1 stores 270 Watt-hours of energy and aircraft 2 stores 45 Watt-hours. Aircraft 1 would deplete its battery after only 18 seconds of flight at maximum velocity. Aircraft 2 would deplete its battery after 73 seconds of flight at its stall velocity.

This analysis shows that while the current research focus on increasing actuator thrust is necessary, if DBD actuators are to be used for more than stall control applications, increasing actuator effectiveness levels is also critical. Otherwise, the only option is to wait for higher energy density storage to become available.

## 6. CONCLUSIONS

It is well known that DBD actuators are not yet able to produce thrust levels sufficient to implement a control system of the kind investigated in this work. The intent of this work was to determine the amount of power that such a system would require if DBD actuator effectiveness levels remain constant while the thrust levels increase. The analysis above shows that the power requirements would be prohibitive to mounting the system on a small aircraft. Under demanding conditions, the aircraft were capable of sustaining trimmed flight for only 18 and 73 seconds of flight, respectively. An improvement in duration could be gained by restricting the flight envelope of the aircraft, but this is undesirable.

The experimental portion of the work does offer some promising results. Actuator thrust and power consumption were investigated for a variety of applied voltages and operating frequencies. It was observed that actuator effectiveness increased as the applied voltage was increased. Because increasing actuator voltage levels has so far been the easiest way to increase actuator thrust, it is possible that actuator effectiveness levels will increase along with increasing thrust.

This suggests that future research should focus on ways to increase actuator effectiveness levels as well as increasing actuator thrust levels. Gaining a more fundamental understanding of actuator operating processes is important to achieving this goal. To this end, future modeling and experimental efforts would do well to focus on DBD plasma formation, plasma quenching, and flow acceleration processes. Novel electrode arrangements, voltage waveforms, or dielectric modifications could also be worthwhile.

Investigations should also be performed from the standpoint of aerodynamic flow control. The jet flap analysis performed above is a brute force technique. Flow modification comes only from the actuator direct momentum addition to the flow. DBD actuators are capable of unsteady forcing and vortex generation; further investigation to exploit these effects could allow actuators to have a greater effect at low power levels.

**BIBLIOGRAPHY**

- [1] Enloe, C., McHarg, M., McLaughlin, T., "Time-correlated force production measurements of the dielectric barrier discharge plasma aerodynamic actuator," *Journal of Applied Physics* 2008, Vol. 103, Article 073302
- [2] Enloe, C., McLaughlin, T., Font, G., "Parameterization of Temporal Structure in the Single-Dielectric-Barrier Aerodynamic Plasma Actuator," *AIAA Journal* 2006, Vol. 44, No. 6, 1127-1136
- [3] Thomas, F., Corke, T., Iqbal, M., Kozlov, A., Schatzman, D., "Optimization of Dielectric Barrier Discharge Plasma Actuators for Active Aerodynamic Flow Control," *AIAA Journal* 2009, Vol. 47, No. 9, 2169-2178
- [4] Opaitis, D., Neretti, G., Zaidi, S., Shneider, M., Miles, R., Likhanskii, A., Macheret, S., "DBD Plasma Actuators Driven by a Combination of Low Frequency Bias Voltage and Nanosecond Pulses," 46th AIAA Aerospace Sciences Meeting and Exhibit, AIAA 2008-1372, Reno, Nevada 2008
- [5] Durscher, R., Roy, S., "Novel Multi-Barrier Plasma Actuators for Increased Thrust," 48th AIAA Aerospace Sciences Meeting Including the New Horizons Forum and Aerospace Exposition, AIAA 2010-965, Orlando, Florida 2010
- [6] Enloe, C., McLaughlin, T., VanDyken, R., Kachner, K., Jumper, E., Corke, T., "Mechanisms and Responses of a Single Dielectric Barrier Plasma Actuator: Plasma Morphology," *AIAA Journal* 2004, Vol. 42, No. 3, 589-594
- [7] Stanfield, S., Menart, J., DeJoseph, C., "Spatially Resolved Optical Emission Spectroscopy Measurements within a Single Microdischarge of a Dielectric Barrier Discharge," 48th AIAA Aerospace Sciences Meeting Including the New Horizons Forum and Aerospace Exposition, AIAA 2010-962, Orlando, Florida 2010
- [8] Stanfield, S., Menart, J., DeJoseph, C., Kimmel, R., Hayes, J., "Rotational and Vibrational Temperature Distributions for a Dielectric Barrier Discharge in Air," *AIAA Journal* 2009, Vol. 47, No. 5, 1107-1115
- [9] Enloe, C., McLaughlin, T., Gregory, J., Medina, R., Miller, W., "Surface Potential and Electric Field Structure in the Aerodynamic Plasma Actuator," 46th AIAA Aerospace Sciences Meeting and Exhibit, AIAA 2008-1103, Reno, Nevada 2008
- [10] Font, G., Enloe, C., Newcomb, J., Teague, A., Vasso, A., McLaughlin, T., "Effects of Oxygen Content on the Behavior of the Dielectric Barrier Discharge Aerodynamic Plasma Actuator," 48th AIAA Aerospace Sciences Meeting Including the New Horizons Forum and Aerospace Exposition, AIAA 2010-545, Orlando, Florida 2010

- [11] Poggie, J., Tilmann, C., Flick, P., Silkey, J., Osborne, B., Ervin, G., Maric, D., Mangalam, S., Mangalam, A., "Closed-Loop Stall Control on a Morphing Airfoil Using Hot-Film Sensors and DBD Actuators," 48th AIAA Aerospace Sciences Meeting Including the New Horizons Forum and Aerospace Exposition, AIAA 2010-547, Orlando, Florida 2010
- [12] Huang, X., Zhang, X., Gabriel, S., "Bluff Body Noise and Flow Control with Atmospheric Plasma Actuators," 29th AIAA Aeroacoustics Conference, AIAA 2008-3044, Vancouver, British Columbia, Canada 2008
- [13] Vincent-Randonnier, A., Larigaldie, S., Magre, P., Sabel'nikov, V., "Experimental Study of a Methane Diffusion Flame Under Dielectric Barrier Discharge Assistance," IEEE Transactions on Plasma Science 2007, Vol. 35, No. 2, 223-232
- [14] Benard, N., Bonnet, J., Touchard, G., Moreau, E. "Flow control by dielectric barrier discharge actuators – Jet mixing enhancement," 4th Flow Control Conference, AIAA 2008-3878, Seattle, Washington 2008
- [15] Post, M., Corke, T., "Separation Control on High Angle of Attack Airfoil Using Plasma Actuators," AIAA Journal 2004, Vol. 42, No. 11, 2177-2184
- [16] Nelson, R., Corke, T., He, C., Othman, H., Matsuno, T., Patel, M., Ng, T., "Modification of the Flow Structure over a UAV Wing for Roll Control," 45th AIAA Aerospace Sciences Meeting and Exhibit, AIAA 2007-884, Reno, Nevada 2007
- [17] Huang, J., Corke, T., Thomas, F., "Plasma Actuators for Separation Control of Low-Pressure Turbine Blades," AIAA Journal 2006, Vol. 44, No. 1, 51-57
- [18] Ozturk, C., Bolitho, M., Jacob, J., "Parametric Study of Thrust Generation in Plasma Microthrusters," 46th AIAA Aerospace Sciences Meeting and Exhibit, AIAA 2008-539, Reno, Nevada 2008
- [19] Morris, C., Corke, T., VanNess, D., Stephens, J., Douville, T., "Tip Clearance Control Using Plasma Actuators," 43rd AIAA Aerospace Sciences Meeting and Exhibit, AIAA 2005-782, Reno, Nevada 2005
- [20] Post, M., Plasma Actuators for Separation Control on Stationary and Oscillating Airfoils, South Bend: Notre Dame, 2004, Dissertation
- [21] Wang, J., Li, H., Liu, F., Luo, S., "Forebody Asymmetric Load Manipulated by a Horseshoe-Shaped Plasma Actuator," 47th AIAA Aerospace Sciences Meeting Including The New Horizons Forum and Aerospace Exposition, AIAA 2009-904, Orlando, Florida 2009
- [22] Post, M., Corke, T., "Flow Control with Single Dielectric Barrier Plasma Actuators," 35th AIAA Fluid Dynamics Conference and Exhibit, AIAA 2005-4630, Toronto, Ontario, Canada 2005
- [23] Zhang, P., Liu, A., Wang, J., "Aerodynamic Modification of a NACA 0012 Airfoil by Trailing-Edge Plasma Gurney Flap," AIAA Journal 2009, Vol. 47, No. 10, 2467-2474

- [24] Corke, T., Tillotson, D., Patel, M., Su, W., Toledo, W., "Radius Flow Vectoring for Projectile Drag and Steering Control Using Plasma Actuators," 4th Flow Control Conference, AIAA 2008-3769, Seattle, Washington 2008
- [25] Corke, T., Enloe, C., Wilkinson, S., "Dielectric Barrier Discharge Plasma Actuators for Flow Control," *Annu. Rev. Fluid Mech.* 2010, Vol. 42, 505-529
- [26] Takagaki, M., Isono S., Nagai, H., Asai, K., "Evaluation of Plasma Actuator Performance in Martian Atmosphere for Applications to Mars airplanes," 4th Flow Control Conference, AIAA 2008-3762, Seattle, Washington 2008
- [27] Abe, T., Takizawa, Y., Sato, S., Kimura, N., "Experimental Study for Momentum Transfer in a Dielectric Barrier Discharge Plasma Actuator," *AIAA Journal* 2008, Vol. 46, No. 9, 2248-2256
- [28] Beckwith, T., Marangoni, R., Lienhard, J., *Mechanical Measurements*, 6<sup>th</sup> edition, Upper Saddle River: Pearson Prentice Hall, 2007
- [29] Spence, D., "The Lift Coefficient of a Thin, Jet-Flapped Wing," *Proceedings of the Royal Society of London. Series A, Mathematical and Physical Sciences* 1956, Vol. 238, No. 1212
- [30] Korbacher, G., "Aerodynamics of Powered High-Lift Systems," *Annu. Rev. Fluid Mech.* 1974, Vol. 6, 319-357
- [31] McKormick, B., *Aerodynamics of V/STOL Flight*, Academic Press, New York, 1967, chapter 7
- [32] Von der Decken, J., "Aerodynamics of Pneumatic High-Lift Devices," *AGARD Lecture Series No. 43*, 1970
- [33] Maskell, E., Spence, D., "A Theory of the Jet Flap in Three Dimensions," *Proceedings of the Royal Society of London. Series A, Mathematical and Physical Sciences* 1959, Vol. 251
- [34] Blakeney, J., *Exploratory Study of the Turning Characteristics of a Coanda-Operated Jet Flap*, Naval Postgraduate School, 1972, Thesis
- [35] Englar, R.J., "Circulation Control Pneumatic Aerodynamics: Blown Force and Moment Augmentation and Modification; Past, Present, & Future," *AIAA Fluids 2000 conference and exhibit*, AIAA 2000-2541, Denver, Colorado 2000

## VITA

Joseph William Ferry was born on May 30, 1986. He currently resides in Rolla, Missouri, where he attends the Missouri University of Science and Technology. In May 2008, Ferry earned a Bachelor of Science in Aerospace Engineering degree from Missouri S&T.

Ferry's professional experience includes two internships with the National Aeronautics and Space Administration. In the summer of 2007, he worked in Huntsville, Alabama, at the Marshall Space Flight Center. He improved a model for predicting liquid propellant rocket engine performance. In the summer of 2008, he worked in Cleveland, Ohio, at the Glenn Research Center where he analysed methods for conducting in-space electronics repair.

